SUPPLEMENTARY INFORMATION

doi:10.1038/nature10981

A review of ion confinement in Penning traps and discussion of a variety of equilibrium states, including 2D Coulomb crystals (ionic Wigner crystals), can be found in [1–3]. A number of authors have theoretically analyzed and discussed the prospects of using 2D Coulomb crystals for quantum information and computation [4–9]. The engineered Ising interaction, which we report here, builds on our previous experimental work using 2D Coulomb crystals for high-fidelity quantum control [10–14]. Below we discuss some details of this new capability.

I. SPIN INITIALIZATION, CONTROL, AND MEASUREMENT

Reference [11] gives a detailed discussion of our spin initialization, control, and measurement capabilities with planar ion arrays in Penning traps. Here we briefly summarize some of that discussion, emphasizing aspects relevant for the measurements reported here. Figure 1 shows the relevant $^9Be^+$ energy levels. We use the valence electron spin states parallel $|\uparrow\rangle = \left|m_J = +\frac{1}{2}\right\rangle$ and antiparallel $|\downarrow\rangle = \left|m_J = -\frac{1}{2}\right\rangle$ to the applied magnetic field of the Penning trap as the two-level system or qubit. In the 4.46 T magnetic field of the trap, these levels are split by approximately $\Omega_0 = 2\pi \times 124$ GHz. The $^9Be^+$ nucleus has spin $I = 3/2$. However, we optically pump the nuclear spin to the $m_I = +3/2$ level [15], where it remains throughout the duration of an experiment. The ions are Doppler laser-cooled to a temperature ~ 1 mK [16] by a 1 MHz linewidth, 313 nm laser tuned approximately 10 MHz below the $|\uparrow\rangle \rightarrow \left|^2P_{3/2}\, m_J = +3/2\right\rangle$ cycling transition. Spins in the $|\downarrow\rangle$ state are efficiently optically pumped to the $|\uparrow\rangle$ state by a laser tuned to the $|\downarrow\rangle \rightarrow \left|^2P_{3/2}\, m_J = +1/2\right\rangle$ transition. The repump beam and the main Doppler laser cooling beam are directed along the magnetic field ($\hat{z}$-axis). Powers are a few milli-Watt with laser beam waists of ~ 1 mm. In addition, a weak Doppler laser cooling beam ($\sim 40\,\mu$m waist) directed perpendicularly to the $\hat{z}$-axis directly Doppler cools the perpendicular degrees of freedom. A typical experimental cycle starts with 10 ms to 20 ms of combined Doppler laser cooling and repumping. The repump laser remains on for another 3 ms after the Doppler cooling laser is turned off. The fidelity of the $|\uparrow\rangle$ state preparation is estimated to be very high ($\gg 99.9\%$) [11].

Low-phase-noise microwave radiation at 124 GHz is used to rotate the spins through the magnetic dipole interaction $\hat{H}_B = g\mu_B \sum_i \vec{B}_\mu(t) \cdot \left(\vec{\sigma}_i/2\right)$, where $\vec{B}_\mu(t)$ is the applied microwave field (predominantly perpendicular to $\hat{z}$), $g \simeq 2$ is the electron g-factor, and μ_B is the Bohr magnetron. The fidelity of a π-pulse was measured to be greater than 99.9% in a random benchmarking experiment [11]. The microwave source consisted of an agile 15.5 GHz source followed by an amplifier multiplier chain with 150 mW output power at 124 GHz. The 15.5 GHz source is obtained by mixing, with a single-side-band mixer, the output of a 15.2 GHz dielectric resonator oscillator (DRO) with the output of a 300 MHz direct digital synthesizer (DDS) that is under field programmable gate array (FPGA) control. On/off switching of the 124 GHz microwaves is done at 15.5 GHz before the amplifier multiplier chain. The microwaves are transported to the ions down the bore of the magnet with a rigid waveguide and directed onto the ions with a horn located between the ring and endcap electrodes of the trap. With this arrangement the microwave hardware does not block optical access along the magnetic field axis, enabling imaging of the ion resonance fluorescence scattered along the magnetic field (top-view image — see III). We obtain π-pulses of $70\,\mu$s duration with the 150 mW output power of the amplifier multiplier chain and the setup described here. The measured spin-echo coherence duration (T_2) is ~ 100 ms.

At the end of an experimental sequence we turn on the Doppler cooling laser and make a projective measurement of the ion spin state through state-dependent resonance fluorescence. With the Doppler cooling laser on, an ion in the $|\uparrow\rangle$ state scatters $\sim 10^7$ photons/s while an ion in $|\downarrow\rangle$ is dark. For the spin precession measurements reported here we performed a global spin-state detection. Specifically we detected, with $f/5$ light collection and a photomultiplier tube, the resonance fluorescence from all the ions in a direction perpendicular to the magnetic field (the side-view). For detection periods of ~ 50 ms the detection fidelity is high, typically limited by quantum projection noise. Here we used short detection periods of $\sim 500\,\mu$s, from which we would detect ~ 1 photon for each bright state $|\uparrow\rangle$. Typically, each experiment was repeated ~ 100 times and averaged, resulting in a few percent uncertainty due to shot noise in the measurement of $P(\uparrow)$.

The spin-precession signal used to benchmark spin-spin coupling in the manuscript relied on a global spin-state measurement via side-view fluorescence collected on a photo-multiplier tube. In the future, we anticipate that time-resolved top-view images such as that shown in Fig. 1 will be used to obtain the spin state of individual ions. As discussed in the manuscript, ion crystal rotation at ω_r is phase-locked locked to an external oscillator. We use an imaging photomultiplier tube to record (x,y,t) for each photon. Rotating-frame images are generated computationally given (x,y,t) and ω_r, a technique established in 2001 [17]. In linear Paul trap experiments, determination of ion spin-state is possible with as few as 10 photons/ion [18]. At present we await the arrival of a new (x,y,t) detector system capable of a detection rate of 5×10^6 Hz. We anticipate this will enable high-fidelity spin-state measurement of a 300-ion crystal in ~ 10 ms. From a suite of identical experiments, the spin-spin correlation function can be computed. We believe that our ability to resolve single ions, even in the presence of rotation at ω_R indicates a path forward in performing individually resolved measurements of fluorescence correlations between ions.

Previous measurements have elucidated some of the possible limiting mechanisms. For instance, the stability of crystal orientation in the rotating frame was studied for spherical crystals of $\sim 10{,}000$ ions. In these experiments the orientation was observed to precess uniformly for durations of $\gtrsim 10$ s, then suddenly slip by a large angle before again resuming slow precession [17]. This "stick-slip" motion can be followed and easily corrected. Figure 1a of the manuscript was generated from 600 s of integration after stick-slip corrections. Other potential issues include ion loss and background gas collisions. As the trap depth is $\gg 1$ eV, background gas collisions do not result ion loss. Collisions with background hydrogen generate BeH^+ (1 per 6 minutes for $N \sim 300$ $^9Be^+$ ions) which collect at the crystal perimeter due to centrifugal separation. These effects do not appear to limit top-view imaging fidelity, as demonstrated in Fig. 1a of the manuscript.

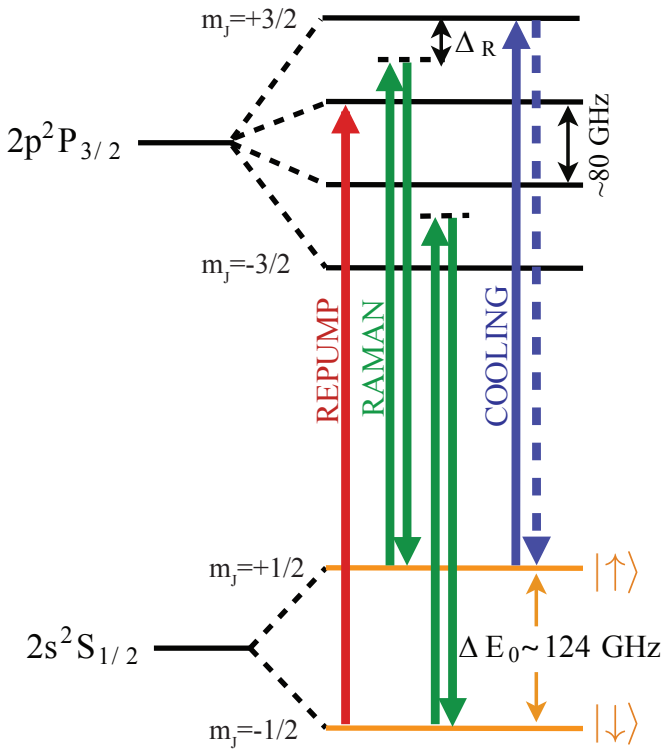

Figure 1. Relevant energy levels of $^9Be^+$ at $B_0 = 4.46$ T (not drawn to scale). We show only $m_I = +\frac{3}{2}$ levels that are prepared experimentally through optical pumping. The $^2S_{1/2} - {}^2P_{3/2}$ transition wavelength is ~ 313 nm. A resonant laser beam provides Doppler laser cooling and state discrimination; a second laser beam repumps $|\downarrow\rangle$ to $|\uparrow\rangle$. The optical dipole force (ODF) interaction is due to a pair of beams (derived from the same laser) with relative detuning μ_R. The qubit splitting $\Delta E_0/\hbar \sim 2\pi \times 124$ GHz. A low-phase-noise microwave source at 124 GHz provides full global control over spins.

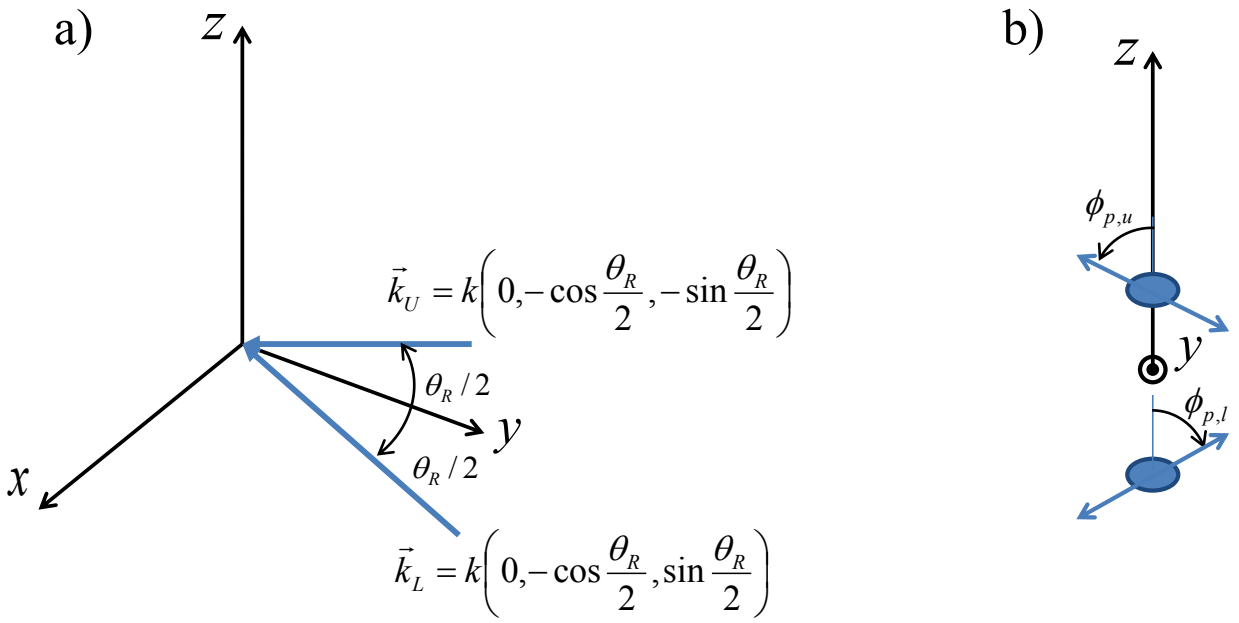

Figure 2. Sketch of optical dipole force (ODF) laser beam setup. (a) The ODF laser beams lie in the y-z plane at angles $\pm\theta_R/2$ with respect to the y-axis. (b) View looking in the $-\hat{y}$ direction. The beams are linearly polarized but with different polarization angles relative to vertical polarization.

II. OPTICAL-DIPOLE-FORCE LASER SETTINGS

Figure 2 shows a simple sketch of the optical dipole force (ODF) laser beam set-up. As discussed below, the frequency as well as the beam polarizations were chosen to null the AC Stark shift from an individual beam and to produce a state-dependent force that is equal in magnitude but opposite in sign for the $|\uparrow\rangle$ and $|\downarrow\rangle$ qubit states ($F_\uparrow = -F_\downarrow$). This reduced the system sensitivity to laser intensity fluctuations. For example, if $F_\uparrow \neq -F_\downarrow$, then the interaction induced by the optical dipole force will include terms linear in the $\hat{\sigma}_i^z$'s. These terms can be canceled with spin-echo techniques, but this requires that laser intensity fluctuations are small. Likewise, by adjusting the laser polarization to null the AC Stark shift from a single beam, we mitigated qubit decoherence due to laser intensity fluctuations. For the benchmarking measurements described here we did not actively stabilize (i.e., noise eat) the laser beam intensity.

The off-resonant laser beam frequency was detuned from the cycling transition $\left(|\uparrow\rangle \rightarrow \left|P_{3/2}, m_J = 3/2\right\rangle\right)$ by $\Delta_R \simeq -63.8$ GHz. This gives detunings of $+15.6$ GHz and -26.1 GHz, respectively, from the $|\uparrow\rangle \rightarrow \left|P_{3/2}, m_J = 1/2\right\rangle$ and $|\downarrow\rangle \rightarrow \left|P_{3/2}, m_J = -1/2\right\rangle$ transitions (Fig. 1). Laser beam waists were $w_z \simeq 110\,\mu$m in the vertical (z-direction) and $w_x \simeq 1$ mm in the horizontal direction. Here we define the waist as the distance from the center of the beam over which the electric field intensity decreases by $1/e^2$ (i.e. $I(z) \sim e^{-(z/w_z)^2}$). With the small 2.4° incident angle each beam makes with respect to the plane of the crystal, this provided a uniform electric field with $< 10\%$ intensity variation across ion crystal arrays with $N < 250$.

The ODF laser beams were linearly polarized at nonzero angles with respect to the $\hat{z}$-axis. Let

$$\begin{aligned} \vec{E}_U(\vec{r},t) &= \hat{\varepsilon}_U E_U \cos\left(\vec{k}_U \cdot \vec{r} - \omega_U t\right) \\ \vec{E}_L(\vec{r},t) &= \hat{\varepsilon}_L E_L \cos\left(\vec{k}_L \cdot \vec{r} - \omega_L t\right) \end{aligned} \tag{1}$$

denote the electric fields of the upper and lower ODF beams. If ϕ_p is the angle of the laser beam electric-field polarization with respect to vertical polarization ($\hat{\varepsilon} \cdot \hat{x} = 0$), then the AC Stark shift of the qubit states when illuminated by a single beam can be written

$$\begin{aligned} \Delta_{\uparrow,acss} &= A_\uparrow \cos^2(\phi_p) + B_\uparrow \sin^2(\phi_p) \\ \Delta_{\downarrow,acss} &= A_\downarrow \cos^2(\phi_p) + B_\downarrow \sin^2(\phi_p) \end{aligned} \tag{2}$$

where $A_\uparrow(A_\downarrow)$ is the Stark shift of the $|\uparrow\rangle(|\downarrow\rangle)$ state for a π-polarized beam ($\hat{\varepsilon}$ parallel to the $\hat{z}$-axis) and $B_\uparrow(B_\downarrow)$ is the Stark shift of the $|\uparrow\rangle(|\downarrow\rangle)$ state for a σ-polarized beam ($\hat{\varepsilon}$ perpendicular to the $\hat{z}$-axis). (Here we neglect the small σ polarization ($\propto \sin 2.4^o$)

that exists when $\phi_p = 0$.) The Stark shift of the qubit transition is

$$\Delta_{acss} = \left(A_\uparrow - A_\downarrow\right)\cos^2(\phi_p) + \left(B_\uparrow - B_\downarrow\right)\sin^2(\phi_p)\ . \tag{3}$$

If $A_\uparrow - A_\downarrow$ and $B_\uparrow - B_\downarrow$ have opposite signs, there is an angle which makes $\Delta_{acss} = 0$. For a laser detuning of $\Delta_R = -63.8$ GHz, $\Delta_{acss} = 0$ at $\phi_p \simeq \pm 65^o$.

With $\Delta_{acss} = 0$ for each ODF laser beam, we exploit the freedom to choose their polarization in order to obtain a state-dependent force. Specifically, we choose $\vec{E}_U$ to have a polarization given by $\phi_{p,u} = 65^o$ and $\vec{E}_L$ to have a polarization given by $\phi_{p,l} = -65^o$. In this case the interference term in the expression for the electric field intensity $\left(\vec{E}_U + \vec{E}_L\right)^2$ produces a polarization gradient which results in spatially dependent AC Stark shifts

$$\begin{array}{l}\left(A_\uparrow\cos^2(\phi_p) - B_\uparrow\sin^2(\phi_p)\right)2\cos\left(\delta k\cdot z - \mu_R t\right)\\ \left(A_\downarrow\cos^2(\phi_p) - B_\downarrow\sin^2(\phi_p)\right)2\cos\left(\delta k\cdot z - \mu_R t\right)\end{array} \tag{4}$$

for the qubit levels. Here $\delta k \equiv \left|\vec{k}_U - \vec{k}_L\right| = 2k\sin\left(\frac{\theta_R}{2}\right)$ is the wave vector difference between the two ODF laser beams, $\mu_R = \omega_U - \omega_L$ is the ODF beat note, and $\phi_p = |\phi_{p,u}| = \left|\phi_{p,l}\right|$. The spatially dependent AC Stark shift produces a state-dependent force $F_{\uparrow,\downarrow}(z,t) = F_{o\uparrow,\downarrow}\sin\left(\delta k\cdot z - \mu_R t\right)$ where

$$\begin{array}{l}F_{o\uparrow} = -2\,\delta k\left(A_\uparrow\cos^2(\phi_p) - B_\uparrow\sin^2(\phi_p)\right)\\ F_{o\downarrow} = -2\,\delta k\left(A_\downarrow\cos^2(\phi_p) - B_\downarrow\sin^2(\phi_p)\right).\end{array} \tag{5}$$

In general $F_{o\uparrow} \neq -F_{o\downarrow}$. We operate at $\Delta_R = -63.8$ GHz where for $\Delta_{acss} = 0$ we also obtain $F_{o\uparrow} = -F_{o\downarrow} \equiv F_o$

For a given $\phi_{p,u}$, $\phi_{p,l}$, and Δ_R we use straightforward atomic physics along with well known values for the energy levels and matrix elements of $^9Be^+$ to calculate F_o as a function of the electric field intensity $I_R = \frac{c\varepsilon_o}{2}|E_L|^2 = \frac{c\varepsilon_o}{2}|E_U|^2$ at the center of the laser beams. For $\theta_R = 4.8^\circ$ and $I_R = 1$ W/cm^2 , $F_o = 1.4\times10^{-23}$ N.

Stronger forces can be generated after experimental modification to our apparatus to permit $\theta_R \approx 35^o$. At this angle larger detunings $\mu_R - \omega_1$ are required to satisfy Eq. 6 in Methods. With our definition $H_I = \frac{1}{N}\sum_{i<j} J_{i,j}\hat{\sigma}_i^z\hat{\sigma}_j^z$, the interaction strength between two ions i and j is $J_{i,j}/N$. Consider for example $N = 217$ ions, $\omega_r = 2\pi\times 45.6$ kHz, powers of $I_R = 20$ mW/beam (12.5 W/cm^2) and $\theta_R = 35^o$. The spin-motion entanglement constraint is satisfied by a detuning of $\mu_R - \omega_1 = 2\pi\times 100$ kHz. In this case we obtain $J_{i,j}/(2\pi N) \sim (560\,Hz)\,(d_0/d_{i,j})^{1.7}$, where $d_0 \sim 20\,\mu$m is the typical nearest neighbor separation.

III. WAVEFRONT ALIGNMENT

The ODF laser beams produce a one dimensional (1D) optical lattice characterized by the effective wave vector $\delta\vec{k}$ and beat note μ_R. In Sec. II we assumed that $\delta\vec{k} \parallel \hat{z}$, or equivalently that the wavefronts of the lattice were aligned perpendicular to the $\hat{z}$-axis (magnetic field axis). If the wavefronts are not normal to the $\hat{z}$-axis as sketched in Fig. 3, then the time dependence of the ODF seen by an ion in the rotating frame depends on the (x,y) position of the ion. This complicates the effective spin-spin interactions generated by the ODF but can be adequately mitigated by careful alignment.

Alignment of the ODF laser beams is obtained by a technique that makes top-view images (images of the ion resonance fluorescence scattered along the magnetic field) from a single plane of ions sensitive to ODF wave front misalignment. For this measurement we set $\mu_R = 0$ (stationary 1D lattice) and detune the frequency of the ODF laser beams approximately 0.5 GHz below the $|\uparrow\rangle \rightarrow \left|^2P_{3/2}\,m_J = +3/2\right\rangle$ Doppler cooling transition. This small detuning generates sufficiently large AC Stark shifts on the cooling transition to measurably change the ion scatter rate from the Doppler cooling laser. With the Doppler cooling laser turned on and the ODF beams turned off, we observe a spatially uniform, time-averaged image of a rotating planar crystal. With the ODF beams on, ions located in regions of high electric field intensity at the anti-nodes of the optical lattice are Stark-shifted out of resonance with the Doppler cooling laser. This is the cause of the dark bands in the top-view image shown in Fig. 4. We adjust the ODF laser beams based on this real-time imaging to optimize their alignment. Improved alignment is indicated by a fringe pattern of longer wavelength. With this technique we have aligned the ODF wave fronts with the planar array to better than $\sim 0.05^\circ$.

The image in Fig. 4 is typical of what we obtain with 1 s integration duration. This indicates the 1D lattice was stable during the integration period and shows the phase stability of our 1D lattice of better than 1 s.

We note that direct fluorescence imaging of the 1D lattice, for example by tuning the ODF laser resonant with the Doppler cooling transition, is not viable. Even at low powers, resonantly scattered photons across the large horizontal waist of the ODF beams apply a large torque, causing the rotation frequency and radius of the array to rapidly change, typically driving the ions into orbits of very large radius.

We have also used phase coherent Doppler velocimetry to improve the ODF wavefront alignment [19]. But the top-view imaging technique discussed here and shown in Fig. 4 provides more information on the angle and direction of misalignment, which greatly improves the ODF-crystal alignment process.

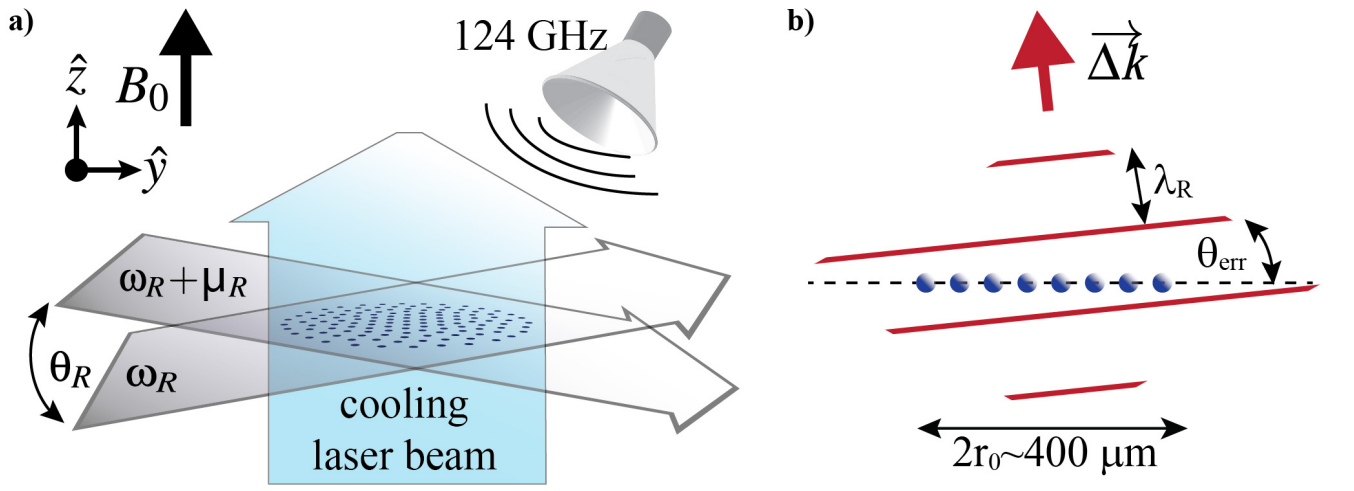

Figure 3. (a) Sketch of the ODF laser beam geometry used to generate the one dimensional (1D) traveling optical lattice. (b) Sketch of the 1D optical lattice wave fronts (red lines). These wave fronts need to be aligned with with the ion planar array (represented by the blue dots). Here $\lambda_R = 2\pi/|\vec{\Delta k}| \approx 3.7\,\mu$m and θ_{err} denotes the angle of misalignment. $400\,\mu$m is the typical array diameter for $N \sim 200$ ions. With the wavefront alignment technique discussed in the text we obtain $\theta_{\rm err} < 0.05°$.

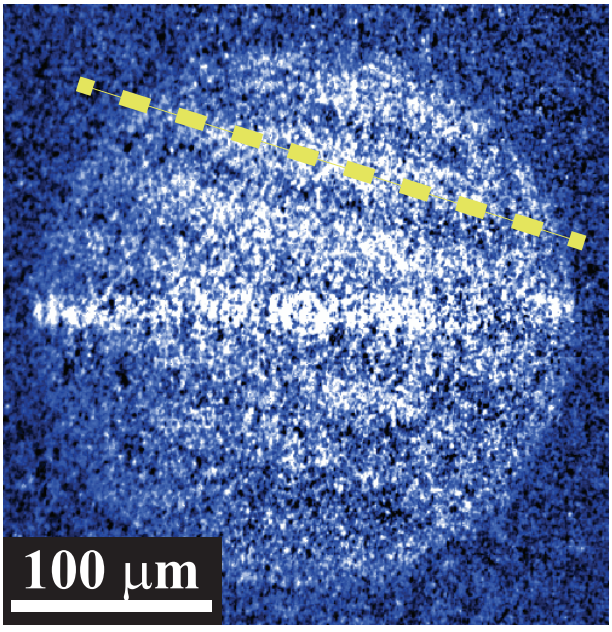

Figure 4. Top-view image of the spatially inhomogeneous fluorescence from a single ion plane produced by the AC Stark shift from a static ($\mu_R = 0$) ODF lattice with misaligned wave fronts. Dark bands are regions of high standing wave electric field intensity (parallel to the dashed yellow line). The bright horizontal feature bisecting the center of the image is fluorescence from the weak Doppler laser cooling beam directed perpendicular to the magnetic field. The image was obtained by subtracting a background image with the ODF beams off (1 s integration).

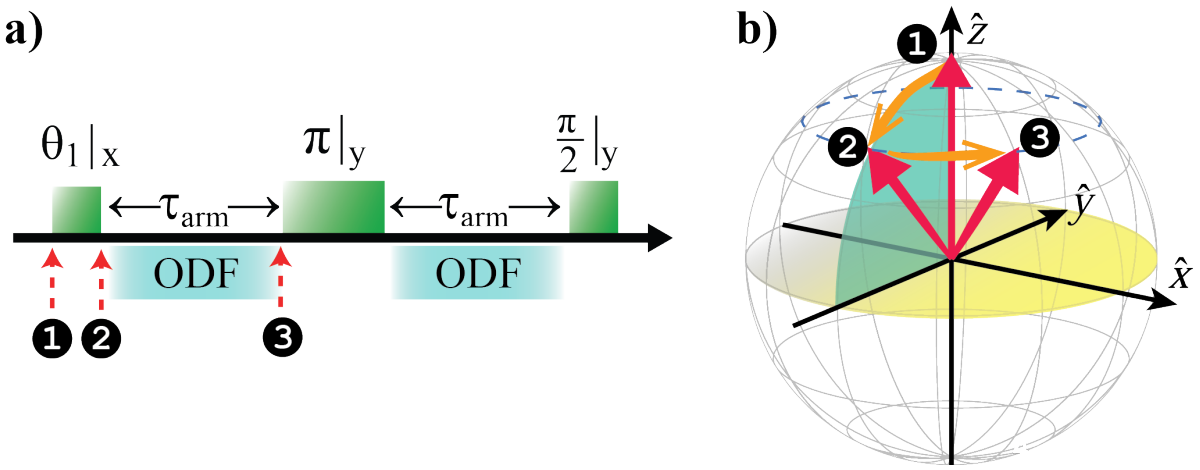

Figure 5. (a) Sequence used to measure spin precession due to the effective mean field generated by the engineered Ising interaction. The spins are initially prepared in $|\uparrow\rangle$. The first pulse rotates the spins by an angle θ_1 about an axis (defined to be the $\hat{x}$-axis in the rotating frame) in the equatorial plane. The subsequent π and $\pi/2$ pulses occur about the $\hat{y}$-axis. (b) Evolution of a single spin prior to the application of the spin-echo π-pulse.

IV. MODELING MEAN FIELD SPIN PRECESSION

For any spin j, $\left[\hat{\sigma}_j^z, \hat{H}_I\right] = 0$, which implies $\left\langle \hat{\sigma}_j^z \right\rangle$ = constant under application of $\hat{H}_I$. The Hamiltonian $\hat{H}_I^{MF}$ describing the mean field response of spin j to the application $\hat{H}_I$ is obtained by expanding $\hat{H}_I$ to first order in $\widehat{\delta\sigma}_j^z \equiv \hat{\sigma}_j^z - \left\langle \hat{\sigma}_j^z \right\rangle$:

$$\begin{aligned} \hat{H}_I^{MF} &= \tfrac{1}{N}\textstyle\sum_{i<j} J_{i,j}\left(\langle\hat{\sigma}_i^z\rangle\,\widehat{\delta\sigma}_j^z + \left\langle\hat{\sigma}_j^z\right\rangle\widehat{\delta\sigma}_i^z\right) \\ &= \textstyle\sum_{j=1}^{N}\tfrac{1}{N}\sum_{i,i\neq j}^{N} J_{i,j}\,\langle\hat{\sigma}_i^z\rangle \times \widehat{\delta\sigma}_j^z. \end{aligned} \tag{6}$$

Defining $\bar{B}_j \equiv \frac{2}{N}\sum_{i,i\neq j}^{N} J_{i,j}\langle\hat{\sigma}_i^z\rangle$, $\hat{H}_I^{MF}$ can be written

$$\hat{H}_I^{MF} = \sum_{j=1}^{N} \bar{B}_j \widehat{\delta\sigma}_i^z/2. \tag{7}$$

The mean field Heisenberg equations of motion for spin $\vec{\sigma}_k$ is obtained from the commutator of $\vec{\sigma}_k$ and $\hat{H}_I^{MF}$. However, because $\widehat{\delta\sigma}_j^z = \hat{\sigma}_k^z - \langle\hat{\sigma}_k^z\rangle$ and $\langle\hat{\sigma}_k^z\rangle$ is a constant, it is clear that Eq. 7 describes spin precession about the z-axis at frequency $\bar{B}_k$. Our observable is the spin precession (in excess of ordinary Larmor precession) averaged over all the spins $\frac{1}{N}\sum_{k=1}^{N}\bar{B}_k$.

We use the spin-echo sequence in Fig. 5 to measure a precession proportional to the expectation value of the spin projection along $\hat{z}$ ($\langle\hat{\sigma}_i^z\rangle$). The spin-echo sequence minimizes contributions to spin precession that are not $\propto\langle\hat{\sigma}_i^z\rangle$. Specifically, the spin echo cancels a constant spin precession independent of $\langle\hat{\sigma}_i^z\rangle$ (e.g., due to slow uncontrolled magnetic field fluctuations), but precession $\propto\langle\hat{\sigma}_i^z\rangle$ coherently adds in the two arms of the sequence.

The first pulse sets $\langle\hat{\sigma}_i^z\rangle = \cos\theta_1$. The interaction $\hat{H}_I$ is then applied by turning on the ODF laser beams for a period τ_{arm}. During this interval $\langle\hat{\sigma}_i^z\rangle$ is a constant and mean field theory predicts an average spin precession angle of $2\bar{J}\cos(\theta_1)\cdot\tau_{arm}$. The π-pulse changes $\langle\hat{\sigma}_i^z\rangle \to -\cos(\theta_1)$ and the spin precession angle $2\bar{J}\cos(\theta_1)\cdot\tau_{arm}$ to $-2\bar{J}\cos(\theta_1)\cdot\tau_{arm}$. At the end of the second $\hat{H}_I$ interaction of duration τ_{arm}, the total precession angle of the spins is $-2\bar{J}\cos(\theta_1)\cdot 2\tau_{arm}$. The final $\pi/2$-pulse is about an axis shifted by 90^o from the first θ_1-pulse. This pulse converts precession out of the initial $\hat{y}\hat{z}$ plane into excursions above or below the equatorial plane of the Bloch sphere, which we measure.

The evolution operator of the measurement sequence $\hat{U}_{seq}$ is obtained in a straight forward manner from the individual evolution operators from each segment of the sequence,

$$\hat{U}_{seq} = \hat{R}\left(\hat{y},\frac{\pi}{2}\right)\cdot\hat{U}\left(\hat{H}_I^{MF}\right)\cdot\hat{R}\left(\hat{y},\pi\right)\cdot\hat{U}\left(H_I^{MF}\right)\cdot\hat{R}\left(\hat{x},\theta_1\right). \tag{8}$$

Here $\hat{R}(\hat{x},\theta_1) = \begin{bmatrix} \cos(\theta_1/2) & -i\sin(\theta_1/2) \\ -i\sin(\theta_1/2) & \cos(\theta_1/2) \end{bmatrix}$, $\hat{R}(\hat{y},\pi) = \begin{bmatrix} 0 & -1 \\ 1 & 0 \end{bmatrix}$ and $\hat{R}\left(\hat{y},\frac{\pi}{2}\right) = \frac{\sqrt{2}}{2}\begin{bmatrix} 1 & -1 \\ 1 & 1 \end{bmatrix}$. The mean field evolution is

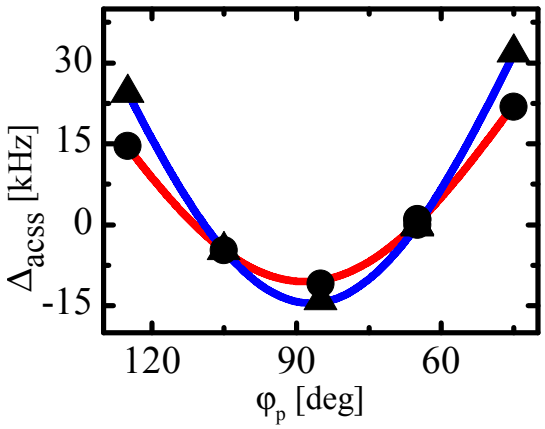

Figure 6. We determine I_R from the AC Stark shift of the qubit transition as a function of ODF laser beam polarization angle ϕ_p. The triangles and filled circles are separate measurements done on the upper and lower ODF beams. I_R is determined independently for each ODF beam by a fit to Eq. 3. The error bars are smaller than the plot points.

given by

$$\hat{U}\left(\hat{H}_I^{MF}\right) = \begin{bmatrix} \exp\left(-i\bar{J}\langle\hat{\sigma}_z\rangle\tau_{arm}\right) & 0 \\ 0 & \exp\left(i\bar{J}\langle\hat{\sigma}_z\rangle\tau_{arm}\right) \end{bmatrix} \tag{9}$$

where $\langle\hat{\sigma}_z\rangle = \cos(\theta_1)$ in the first arm of the spin-echo sequence and $\langle\hat{\sigma}_z\rangle = -\cos(\theta_1)$ in the second arm. At the end of the sequence we detect the $|\uparrow\rangle$ state probability. Explicit computation gives

$$\left|\langle\uparrow|\hat{U}_{seq}|\uparrow\rangle\right|^2 = \frac{1}{2}\left\{1+\sin(\theta_1)\cdot\sin\left[2\bar{J}\cos(\theta_1)\cdot 2\tau_{arm}\right]\right\}. \tag{10}$$

V. OPTICAL DIPOLE FORCE LASER INTENSITY CALIBRATION

The spin-spin couplings ($\bar{J}$) measured here depend on the square of the ODF electric field intensity I_R. Therefore, careful calibration of the electric field intensity was important in benchmarking the strength of the interactions with mean-field predictions. We separately determined I_R for each beam by measuring the AC Stark shift of the qubit transition as a function of the laser beam polarization angle ϕ_p, as shown in Fig. 6. The qubit transition frequency was measured by fitting for the center frequency of a Rabi-resonance profile. The polarization angle ϕ_p was varied by rotating a $\lambda/2$ plate. The Stark shift measurements were fit to Eq. 3, which provided values for A and B (Stark shifts for π-polarization and σ-polarization). Values for A and B were then used with atomic physics calculations to determine I_R, the electric field intensity of the ODF laser beams, with a fractional uncertainty of $\sim 5\%$. Frequent intensity calibration measurements were taken during a benchmarking run. Slow drifts to the laser intensity between calibrations added another 5% uncertainty, which we add in quadrature to the fitted uncertainty.

VI. SPONTANEOUS EMISSION

Decoherence due to spontaneous emission has been well studied in this system [14]. The qubit levels are closed under spontaneous light scattering; that is, spontaneous light scattering does not optically pump the ion to a different ground state level outside of the two qubit levels. We measure spin precession to benchmark the Ising interaction couplings. Equivalently we measure the evolution of off-diagonal coherences between the $|\uparrow\rangle$ and $|\downarrow\rangle$ levels. Spontaneous-emission-induced decay of these coherences is accurately modeled by Eq. (8) of Ref. [14]. We add this time dependence to the unitary evolution $\hat{U}\left(\hat{H}_I^{MF}\right)$ discussed in Sec. IV. This results in the expression

$$P(|\uparrow\rangle) = \frac{1}{2}\left(1+\exp(-\Gamma\cdot 2\tau_{arm})\sin(\theta_1)\sin\left(2\bar{J}\cos(\theta_1)\cdot 2\tau_{arm}\right)\right), \tag{11}$$

where $P(|\uparrow\rangle)$ is the probability of detecting a spin in $|\uparrow\rangle$ at the end of the spin-echo sequence. The only difference with Eq. 10 is the factor $\exp(-\Gamma\cdot 2\tau_{arm})$ due to the decay of the off-diagonal elements of the density matrix. Here Γ accounts for decoherence due to spontaneous emission. From [14], $\Gamma = \frac{1}{2}(\Gamma_{Ram}+\Gamma_{el})$ has contributions from both Raman scattering and elastic Rayleigh

scattering. A straightforward atomic physics calculation relates Γ to the ODF laser beam intensity I_R. In fits of Eq. 11 to the spin-precession measurements, we fix Γ at the value determined by the laser intensity calibrations. For $\Delta_R = -63.8$ GHz, $\phi_p = \pm 65.3^o$, and $I_R = 1$ W/cm^2, we calculate $\Gamma = 82$ s^{-1}.

With our present set-up we can achieve $\bar{J} \gg \Gamma$ for detunings $|\mu_R - \omega_1| \lesssim 10$ kHz. For these detunings it will be possible to simulate quantum effects beyond mean field theory such as spin squeezing and spin-depolarization due to many-body interactions. For example we calculate that with 4 mW/beam and an ODF beatnote detuning of $|\mu_R - \omega_1| = 2$ kHz , $\bar{J} \sim 2\pi \times 0.5$ kHz and $\Gamma/\bar{J} \sim 0.06$. The potential spin squeezing due to this interaction is 5 dB, limited by spontaneous emission. For many simulations it will be desirable to achieve $J/N \gg \Gamma$ where J is a nearest-neighbor coupling strength. ($J \sim \bar{J}$ for small detunings $|\mu_R - \omega_1|$.) The most straight forward strategy to achieve this condition in our set-up appears to be to increase the angle θ_R between the Raman beams. The ratio $\bar{J}/\Gamma$ scales as $\sin^2(\theta_R/2)$. Therefore decoherence due to spontaneous emission can be dramatically reduced with an order of magnitude increase in θ_R. We note that a large increase in θ_R will require implementation of a sub-Doppler cooling scheme to remain in the Lamb-Dicke regime (see Sec. VII).

Different ODF laser detunings can likely help reduce the impact of spontaneous emission (with the complication that $F_\uparrow \neq -F_\downarrow$), but very large laser detunings Δ obtained by tuning the ODF laser beam frequencies outside the $P_{1/2} - P_{3/2}$ manifold appear unlikely to help. This is because both the interaction strength and spontaneous emission scale as $1/\Delta^2$ for our qubit, which is not a clock transition. For trapped-ion experiments in low magnetic field, the impact of spontaneous emission is typically minimized by tuning the ODF laser beam frequencies between the $P_{1/2}$ and $P_{3/2}$ manifolds. Because the ^{9}Be$^+$ P-state fine structure (197 GHz) is comparable to the Zeeman splittings for our magnetic field (4.5 T), this approach does not significantly help. However, it can help with heavier mass ions (e.g., Mg$^+$). Reference [9] discusses a number of strategies that can minimize the impact of spontaneous emission when the P-state fine structure is large compared to the Zeeman interaction energy.

VII. LAMB-DICKE CONFINEMENT

Throughout this manuscript we implicitly assume that the applied state-dependent force, $F_{\uparrow,\downarrow}(z,t) = F_{o\uparrow,\downarrow}\cos(\delta k \cdot z - \mu_R t)$, is constant across the spatial extent of an ion's wave function. Specifically, for a planar array located at $z = 0$, we assume the force on any ion is given by

$$F_{\uparrow,\downarrow}(z=0,t) = F_{o\uparrow,\downarrow}\cos(\mu_R t)\ . \tag{12}$$

The extent to which this is true is quantified by the parameter

$$\eta_{ind,i} \equiv \delta k \cdot z_{rms,i} \tag{13}$$

where $z_{rms,i}$ is the root mean square (rms) axial extent of the wave function of ion i and $\delta k \equiv 2\pi/\lambda_R$, where $\lambda_R = 3.7\,\mu$m for $\theta_R = 4.8^o$. We note that $\eta_{ind,i}$ is a Lamb-Dicke *confinement* parameter for a individual ion (ind), not to be confused with the usual Lamb-Dicke parameter that is defined in terms of the ground-state wave function. In the limit that the Coulomb interaction energy between ions is a small perturbation to the axial potential of the trap, we can think of each ion as a single ion confined in the external trap potential, and approximate $z_{rms,i} \simeq \sqrt{\frac{\hbar}{2M\omega_z}} \cdot \sqrt{2\bar{n}+1}$, where M is the mass of an individual ion. Recently we have completed careful axial temperature measurements for single-plane ion crystals [16]. We find ~ 1 mK for the axial COM mode and ~ 0.4 mK for the higher order transverse modes. For $\omega_z = 2\pi \cdot 795$ kHz and conservatively assuming $T = 1$ mK, we calculate $\bar{n} \simeq 26$, $z_{rms,i} \simeq 190$ nm, and $\eta_{ind,i} \simeq 0.32$.

For the benchmarking measurements described here we typically set the rotation frequency of the ion array about ~ 0.5 kHz below the rotation frequency of the $1 \leftrightarrow 2$ plane transition, determined experimentally from side-view images [2]. In this case, the spectrum of the transverse (axial) modes is broad, and we underestimate $z_{rms,i}$ in the above analysis. An improved estimate of $z_{rms,i}$ is obtained by summing the contributions from all of the transverse modes m

$$z_{rms,i} = \left(\sum_m (b_{i,m})^2 \frac{\hbar}{2M\omega_m}(2\bar{n}_m + 1)\right)^{1/2}, \tag{14}$$

where $\bar{n}_m \simeq k_B T/\hbar\omega_m$ is the mean thermal occupation of mode m. We assume here that every mode is characterized by the same temperature T. For $N = 217$ and $\omega_z = 2\pi \times 795$ kHz, the rotation frequency of the $1 \leftrightarrow 2$ plane transition is $\omega_r = 2\pi \times 46.1$ kHz. For $\omega_R = 2\pi \times 45.6$ kHz, the spectrum of the axial modes ranges from 795 kHz down to 224 kHz. With Eq. 14 we calculate $z_{rms,i} \simeq 520$ nm in the center of the array, decreasing to $z_{rms,i} \simeq 250$ nm at the array edge, corresponding to $\eta_{ind,i} \simeq 0.89$ for i near the array center and $\eta_{ind,i} = 0.42$ for i near the array boundary.

The wavefront alignment discussed in a previous section can be viewed as achieving a type of Lamb-Dicke confinement. Let θ_{err} denote the angle of misalignment between the planar array and the ODF 1D lattice (Fig. 3). Relative to the ODF

lattice wavefronts, the rotation of the array produces a time-dependent shift in the axial position of an ion that can be written as $z(t) = R\sin(\theta_{err})\sin(\omega_r t + \varphi)$. Here R is the distance of the ion from the center of the array, and φ is determined by the azimuthal position of the ion in the array. The force on this ion is then

$$F_{\uparrow,\downarrow}(t) = F_{o\uparrow,\downarrow}\cos\left(\delta k R\sin\theta_{err}\cdot\sin(\omega_r t+\varphi) - \mu_R t\right). \tag{15}$$

For Eq. 15 to approximate Eq. 12, we desire $\delta k \cdot 2R_P \sin\theta_{err} < 1$, where R_P is the array radius. For $R_p \simeq 200\,\mu$m (typical for $N = 200$) and $\theta_{err} \simeq 0.05^\circ$ (see Wavefront alignment section), we calculate $\delta k \cdot 2R_P \sin\theta_{err} \approx 0.6$.

VIII. ION LATTICE CONFIGURATION AT EQUILIBRIUM AND TRANSVERSE NORMAL MODES

The ion equilibrium positions $\vec{r}_i$ at zero temperature are calculated by minimizing the Euler-Lagrange action for the Penning trap potentials and the constraint that the ions lie in a plane (at $z = 0$). The solution is a triangular lattice with a lattice constant that increases as one moves radially outward, that has a smooth unfaceted edge and exhibits a degradation in orientational order near the crystal perimeter. The transverse (along $\hat{z}$) phonon modes (ω_m, $\vec{b}_m$) are obtained by Taylor expansion of the potential about the ion equilibrium positions $\vec{r}_i$. In-plane modes (along $\hat{x},\hat{y}$) can also be calculated, by solving a quadratic eigenvalue problem (due to inclusion of the centrifugal and Coriolis forces). The details of the transverse mode calculation is discussed in this section. The problem has also been solved for longitudinal and transverse modes in 1D (e.g., [20, 21]).

In general, the Lagrangian for a collection of N ions with charge q and mass M in an electromagnetic field $\phi_i - \vec{A}(\vec{r}_i)$ is

$$L = T - V = \sum_{i=1}^{N}\left\{\frac{1}{2}M\dot{\vec{r}}_i^{\,2} - q\left(\phi_i - \vec{A}(\vec{r}_i)\cdot\dot{\vec{r}}_i\right)\right\}, \tag{16}$$

where $\vec{r}_i = (r_i, \theta_i, z_i)$ is the coordinate of ion i. In a Penning trap, the field consists of a uniform magnetic field in the $\hat{z}$-direction ($\vec{B} = B_0\hat{z}$) and a harmonic trapping (anti-trapping) electric potential in the $\hat{z}$-direction ($\hat{r}$-direction) with frequency ω_1. Lastly, an additional external time-dependent electric quadrupole potential (the "rotating wall", amplitude V_{wall} at the ions) is applied to control the ion's rotation frequency in the trap [22]. Thus, the scalar potential for ion i is

$$\begin{aligned} q\phi_i &= q\phi_{trap,i} + q\phi_{wall,i} + q\phi_{Coulomb,i} \\ &= \tfrac{1}{2}M\omega_1^2(z_i^2 - r_i^2/2) + V_{wall}r_i^2\cos 2(\theta_i + \omega_r t) + \tfrac{1}{2}k\textstyle\sum_{j\neq k}^{N} q^2/|\vec{r}_{j,k}|, \end{aligned} \tag{17}$$

where the ion-ion separation is $\vec{r}_{j,k} = \vec{r}_j - \vec{r}_k$ and $k = 1/4\pi\varepsilon_0$. Since $\vec{B}$ is uniform, the vector potential energy is

$$q\vec{A}(\vec{r}_i) = -\frac{q}{2}\vec{r}_i \times \vec{B}. \tag{18}$$

The position of the ions at equilibrium is calculated as follows. We move to a rotating frame where the ions' coordinates are stationary by using the coordinate transformation $\vec{r}'_i = (r'_i, \theta'_i, z'_i) = (r_i, \theta + \omega_r t, z_i)$, a counterclockwise rotation. The ions' equilibrium positions $\vec{r}'_i$ can be found by solving the transformed Euler-Lagrange equations L'. To seed the numerical solution, we supply an initial guess for the 2D crystal: a regular, triangular lattice. Consistent convergence requires ion numbers N corresponding to closed shells (e.g., $N = 127$ has six closed shells). We find ion equilibrium positions that deviate from a perfect triangular lattice near the crystal periphery and which have an overall ellipticity due to V_{wall}.

Given $\vec{r}'_i$, the crystal's transverse eigenmodes can be calculated by Taylor expansion of the potential about the equilibrium positions $\vec{r}'_i$. The Lagrangian is

$$L' = \frac{1}{2}\sum_{i=1}^{N} M\dot{z}'_i\dot{z}'_j - \frac{1}{2}\sum_{i,j=1}^{N} K_{ij}z'_i z'_j \tag{19}$$

where z'_i is the axial displacement of i-th ion and $K_{ij} = K_{ji}$ is the symmetric stiffness matrix evaluated for the equilibrium configuration as

$$K_{ij} = \begin{cases} M\omega_1^2 - \displaystyle\sum_{n=1}^{N}\frac{kq^2}{|z'_{ni}|^3} & i = j, n \neq i \\ \dfrac{kq^2}{|\vec{r}'_{ij}|^3} & i \neq j \end{cases}. \tag{20}$$

By minimizing the action $\delta \int dtL' = 0$ with respect to the rotating frame axial coordinates z_i', we obtain N equations of motion

$$\ddot{z}_i' + \sum_{j=1}^{N} \frac{K_{ij}}{M} z_j' = 0, \text{ for } i = 1,2,...,N. \tag{21}$$

Following standard normal mode analysis, the solution is obtained by calculating the eigenmodes of the matrix K_{ij}/M. The result is N eigenvalues ω_m^2, for $m = 1,2,...,N$ (with corresponding frequencies ω).

IX. LIMITS TO THE VALIDITY OF MEAN FIELD THEORY

Here we calculate the domain over which a mean field theory (MF) treatment of $\hat{J}_z^2$ is valid. In the special case of uniform Ising coupling (e.g., $0 < \mu_R - \omega_1 \ll \omega_1 - \omega_2$), we have

$$\hat{H}_I = \frac{2\chi}{N} \left(\sum_{i=1}^{N} \hat{\sigma}_i^z/2 \right) \left(\sum_{j=1}^{N} \hat{\sigma}_j^z/2 \right) = \frac{2\chi}{N} \hat{J}_z^2, \tag{22}$$

where we have neglected a constant offset and $\hat{J}_z = \sum_{i=1}^{N} \hat{\sigma}_i^z/2$ is the z-component of the total composite spin of the system. The interaction strength χ is independent of ion-ion separation and is given by

$$\chi \approx \frac{F_0^2}{\hbar 2M} \frac{1}{\mu_R^2 - \omega_1^2}. \tag{23}$$

We start each experiment with N spins all prepared in the $|\uparrow\rangle$ state. Here we use the composite spin picture where this state is labeled $|J = N/2, M_J = N/2\rangle$. (Formally $|J, M_J\rangle$ labels a state that is an eigenstate of $\hat{\vec{J}}^2$ and $\hat{J}_z$ with eigenvalues $J(J+1)$ and M_J, where $\hat{\vec{J}} = \sum_i \vec{\hat{\sigma}}_i/2$ is the total system spin.) The first pulse of the spin-precession measurement sequence rotates the composite Bloch vector by an angle θ_1. After the rotation by θ_1 the state can be written as

$$|\psi\rangle = \sum_{M_J=-N/2}^{N/2} C(J, M_J) |J, M_J\rangle, \tag{24}$$

where the coefficients $C(J, M_J)$ are significantly non-zero for a small range ΔM_J centered on $M_J^{(0)}$, where $M_J^{(0)} \approx \frac{N}{2} \cos\theta_1$. For a coherent spin state, $\Delta M_J \lesssim \sqrt{N}$.

We want to establish that a $\hat{J}_z^2$ interaction looks like precession $\propto M_J^{(0)}$, at least over short durations. A precession by an angle ϕ about the z-axis is obtained with the operation $e^{-i\phi\hat{J}_z}$,

$$e^{-i\phi\hat{J}_z} |\psi\rangle = \sum_{M_J} C(J, M_J) e^{-i\phi\hat{J}_z} |J, M_J\rangle . \tag{25}$$

We measure expectation values of the total system spin $\hat{\vec{J}}$. It is sufficient therefore to consider how these expectation values transform under the rotation $e^{i\phi\hat{J}_z}$,

$$\langle\psi| \hat{J}_y |\psi\rangle \;\rightarrow\; \langle\psi| e^{i\phi\hat{J}_z} \hat{J}_y e^{-i\phi\hat{J}_z} |\psi\rangle . \tag{26}$$

For simplicity, only matrix elements of the total spin in the $\hat{y}$-direction $\hat{J}_y$ are considered. Identical expressions are also obtained for $\hat{J}_x$.

$$\begin{aligned} &\langle\psi| \hat{J}_y |\psi\rangle \\ &= \textstyle\sum_{M_J', M_J} C(J, M_J')^\star C(J, M_J) \left\langle J, M_J' \middle| \hat{J}_y \middle| J, M_J \right\rangle \\ &= \textstyle\sum_{M_J} \big\{ C(J, M_J - 1)^\star C(J, M_J) \langle J, M_J - 1| \hat{J}_y |J, M_J\rangle \\ &\quad + C(J, M_J + 1)^\star C(J, M_J) \langle J, M_J + 1| \hat{J}_y |J, M_J\rangle \big\} . \end{aligned} \tag{27}$$

The double sum is eliminated by making use of the property that $\hat{J}_y$ has only non-zero matrix elements between states with $M_J^{'} - M_J = \pm 1$. $C(J, M_J \pm 1)$ can be defined to be 0 if $M_J - 1 = -N/2 - 1$ or $M_J + 1 = N/2 + 1$. Similarly

$$\begin{aligned} &\langle\psi| e^{i\phi\hat{J}_z}\hat{J}_y e^{-i\phi\hat{J}_z} |\psi\rangle \\ &= \textstyle\sum_{M_J^{'},M_J} C(J,M_J^{'})^{\star} C(J,M_J) e^{iM_J^{'}\phi} e^{-iM_J\phi} \left\langle J, M_J^{'} \left| \hat{J}_y \right| J, M_J \right\rangle \\ &= \textstyle\sum_{M_J} \left\{ C(J,M_J-1)^{\star} C(J,M_J) e^{-i\phi} \langle J, M_J - 1| \hat{J}_y |J, M_J\rangle \right. \\ &\qquad \left. + C(J,M_J+1)^{\star} C(J,M_J) e^{i\phi} \langle J, M_J + 1| \hat{J}_y |J, M_J\rangle \right\} . \end{aligned} \tag{28}$$

This is to be compared with the same matrix element under the $H_I = \frac{2\chi}{N}\hat{J}_z^2$ interaction,

$$\begin{aligned} &\langle\psi| e^{i\frac{2\chi}{N}\hat{J}_z^2 t}\hat{J}_y e^{-i\frac{2\chi}{N}\hat{J}_z^2 t} |\psi\rangle \\ &= \textstyle\sum_{M_J^{'},M_J} C(J,M_J^{'})^{\star} C(J,M_J) e^{i\frac{2\chi}{N}\left(M_J^{'}\right)^2 t} e^{-i\frac{2\chi}{N}(M_J)^2 t} \left\langle J, M_J^{'} \left| \hat{J}_y \right| J, M_J \right\rangle \\ &= \textstyle\sum_{M_J} \left\{ C(J,M_J-1)^{\star} C(J,M_J) e^{-i\frac{2\chi}{N}(2M_J-1)t} \langle J, M_J - 1| \hat{J}_y |J, M_J\rangle \right. \\ &\qquad \left. + C(J,M_J+1)^{\star} C(J,M_J) e^{i\frac{2\chi}{N}(2M_J+1)t} \langle J, M_J + 1| \hat{J}_y |J, M_J\rangle \right\} . \end{aligned} \tag{29}$$

Equation 29 approximates a rotation about the $\hat{z}$-axis (that is, approximates Eq. 28) if $\frac{2\chi}{N}t\,(2M_j - 1) \approx \frac{2\chi}{N}t\,(2M_j + 1) \approx \frac{2\chi}{N}t \cdot 2M_J^{(0)}$ for all M_J for which $C(J, M_J)$ is significantly non-zero. This is satisfied for short periods t satisfying $\frac{2\chi}{N}t \cdot 2\,(\Delta M_J) \ll 1$. For the initial coherent spin state, $\Delta M_J \lesssim \sqrt{N}$, which puts a limit

$$\chi t \ll \frac{\sqrt{N}}{4} \tag{30}$$

on the period t for which the $\hat{J}_z^2$ interaction can be approximated as a precession $\propto M_J^{(0)}$. The precession frequency predicted by the $\hat{J}_z^2$ analysis, $\frac{2\chi}{N} \cdot 2M_J^{(0)} = \frac{2\chi}{N} \cdot 2\frac{N}{2}\cos\theta = 2\chi\cos\theta$, is in agreement with the precession frequency predicted by the MF analysis.

Equation 30 provides a limit on the period for which the MF analysis is valid. We confirm this limit through explicit calculation of the spin precession benchmarking sequence for the $\hat{H}_I = \frac{2\chi}{N}\hat{J}_z^2$ interaction with $N = 5$, 50 and 100 spins. The exact calculation is possible because the system remains in the symmetric subspace (dimension of Hilbert space is $2N + 1$). Figure 7(a) shows the results of the calculation for five spins. Reasonable agreement between the MF precession formula (Eq. 11 with $\Gamma = 0$) and the exact calculation is obtained for $\chi t = 0.2$, but not for $\chi t = 0.8$ and 1.6, as expected from Eq. 30. Figures 7(b) and 7(c) compare the exact calculation with the MF formula for $N = 50$ and 100 spins. Excellent agreement between the MF formula and the exact calculation is obtained for $\chi t = 0.2$ and 0.8. Some differences are observed at $\chi t = 1.6$. These differences decrease as N increases.

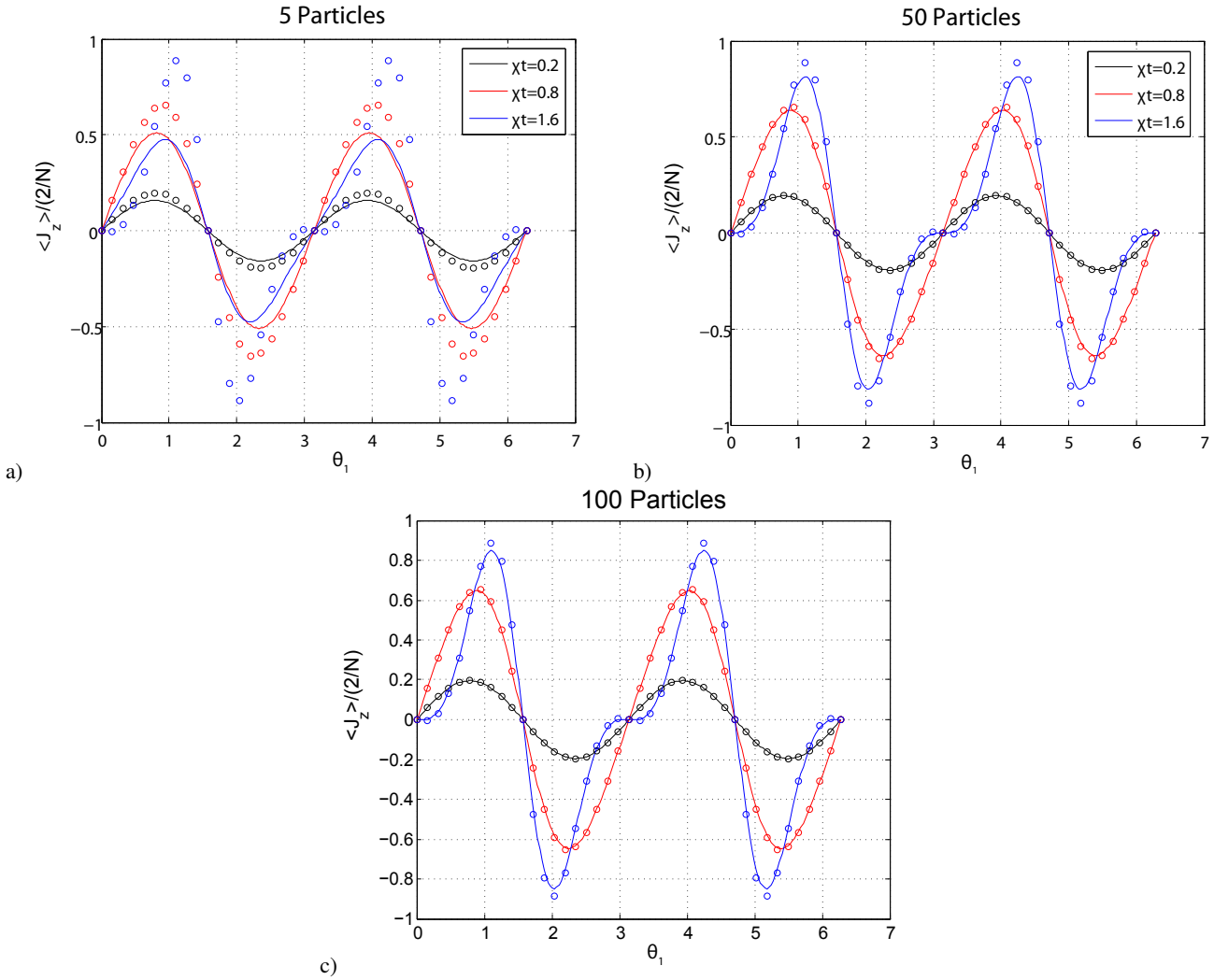

Figure 7. $\langle \hat{J}_z \rangle$ vs initial polar angle θ_1 for an initial coherent spin state of N spins. $t = 2\tau_{arm}$ in the legend is the total interaction period. The solid line is the exact calculation. The open circles are from the MF precession formula (Eq. 11, with $\Gamma = 0$). (a) $N = 5$. (b) $N = 50$. (c) $N = 100$.

[1] Brewer, L. *et al.* Static properties of a non-neutral 9Be+ ion plasma. *Physical Review A* **38**, 859 (1988).

[2] Mitchell, T. *et al.* Direct observations of structural phase transitions in planar crystallized ion plasmas. *Science (New York, N.Y.)* **282**, 1290–3 (1998).

[3] Dubin, D. H. E. & O Neil, T. M. Trapped nonneutral plasmas, liquids, and crystals (the thermal equilibrium states). *Reviews of Modern Physics* **71**, 87–172 (1999).

[4] Porras, D. & Cirac, J. I. Effective Quantum Spin Systems with Trapped Ions. *Physical Review Letters* **92**, 1–4 (2004).

[5] Porras, D. & Cirac, J. Quantum manipulation of trapped ions in two dimensional coulomb crystals. *Physical Review Letters* **96**, 250501 (2006).

[6] Buluta, I., Kitaoka, M., Georgescu, S. & Hasegawa, S. Investigation of planar coulomb crystals for quantum simulation and computation. *Physical Review A* **77**, 1–8 (2008).

[7] Taylor, J. & Calarco, T. Wigner crystals of ions as quantum hard drives. *Physical Review A* **78** (2008).

[8] Zou, P., Xu, J., Song, W. & Zhu, S.-L. Implementation of local and high-fidelity quantum conditional phase gates in a scalable two-dimensional ion trap. *Physics Letters A* **374**, 1425–1430 (2010).

[9] Baltrusch, J., Negretti, A., Taylor, J. & Calarco, T. Fast and robust quantum computation with ionic Wigner crystals. *Physical Review A* **83**, 042319 (2011).

[10] Biercuk, M. J. *et al.* Optimized dynamical decoupling in a model quantum memory. *Nature* **458**, 996–1000 (2009).

[11] Biercuk, M. J. *et al.* High-fidelity quantum control using ion crystals in a Penning trap. *Quantum Information and Computation* **9**, 920–949 (2009).

[12] Biercuk, M. J. *et al.* Experimental Uhrig dynamical decoupling using trapped ions. *Physical Review A* **79**, 062324 (2009).

[13] Uys, H., Biercuk, M. J. & Bollinger, J. J. Optimized noise filtration through dynamical decoupling. *Physical Review Letters* **103**, 40501 (2009).

[14] Uys, H. *et al.* Decoherence due to elastic Rayleigh scattering. *Physical Review Letters* **105**, 200401 (2010).

[15] Itano, W. M. & Wineland, D. J. Precision measurement of the ground-state hyperfine constant of 25Mg+. *Physical Review A* **24**, 1364–1373 (1981).

[16] Sawyer, B. C. *et al.* Spectroscopy and thermometry of drumhead modes in a mesoscopic trapped-ion crystal using entanglement (2012). arXiv:1201.4415v1.

[17] Mitchell, T. B., Bollinger, J. J., Itano, W. M. & Dubin, D. H. E. Stick-slip dynamics of a stressed ion crystal. *Physical Review Letters* **87**, 183001 (2001).

[18] Itano, W. M. & Leibfried, D. Experimental issues in coherent quantum-state manipulation of trapped atomic ions. *Journal Of Research Of The National Institute Of Standards And Technology* **103**, 259–328 (1998).

[19] Biercuk, M. J., Uys, H., Britton, J. W., VanDevender, A. P. & Bollinger, J. J. Phase-coherent detection of an optical dipole force by Doppler velocimetry. *Optics Express* **19**, 10304 (2011).

[20] James, D. Quantum dynamics of cold trapped ions with application to quantum computation. *Applied Physics B: Lasers and Optics* **66**, 181–190 (1998).

[21] Marquet, C., Schmidt-Kaler, F. & James, D. Phonon-phonon interactions due to non-linear effects in a linear ion trap. *Applied Physics B: Lasers and Optics* **76**, 199–208 (2003).

[22] Bollinger, J. J. *et al.* Crystalline order in laser-cooled, non-neutral ion plasmas. *Physics of Plasmas* **7**, 7 (2000).